

## GAMMA-RAY BURSTS FROM MAGNETIZED COLLISIONALLY-HEATED JETS

INDREK VURM,<sup>1,2,3</sup> ANDREI M. BELOBORODOV,<sup>4,5</sup> AND JURI POUTANEN<sup>3</sup>

<sup>1</sup>Racah Institute of Physics, Hebrew University of Jerusalem, Jerusalem 91904, Israel; indrek@phys.huji.ac.il

<sup>2</sup>Tartu Observatory, Tõravere 61602, Tartumaa, Estonia

<sup>3</sup>Astronomy Division, Department of Physics, P.O.Box 3000, 90014 University of Oulu, Finland; juri.poutanen@oulu.fi

<sup>4</sup>Physics Department and Columbia Astrophysics Laboratory, Columbia University, 538 West 120th Street New York, NY 10027; amb@phys.columbia.edu

<sup>5</sup>Astro-Space Center of Lebedev Physical Institute, Profsojuznaja 84/32, Moscow 117810, Russia

*Draft version February 15, 2019*

### ABSTRACT

Jets producing gamma-ray bursts (GRBs) are likely to carry a neutron component that drifts with respect to the proton component. The neutron-proton collisions strongly heat the jet and generate electron-positron pairs. We investigate radiation produced by this heating using a new numerical code. Our results confirm the recent claim that collisional heating generates the observed Band-type spectrum of GRBs. We extend the model to study the effects of magnetic fields on the emitted spectrum. We find that the spectrum peak remains near 1 MeV for the entire range of the magnetization parameter  $0 < \varepsilon_B < 2$  that is explored in our simulations. The low-energy part of the spectrum softens with increasing  $\varepsilon_B$ , and a visible soft excess appears in the keV band. The high-energy part of the spectrum extends well above the GeV range and can contribute to the prompt emission observed by *Fermi*/LAT. Overall, the radiation spectrum created by the collisional mechanism appears to agree with observations, with no fine-tuning of parameters.

*Subject headings:* gamma-ray burst: general — gamma rays: general — radiation mechanisms: non-thermal

### 1. INTRODUCTION

Gamma-ray bursts (GRBs) are produced by ultra-relativistic jets from short-lived and powerful energy sources, probably associated with black hole formation. Apart from the jet launching itself, a primary question of GRB theory concerns the emission mechanism of the burst: how does the jet emit the observed gamma-rays?

The jet must develop an ultra-relativistic speed if its initial thermal energy is much larger than its rest-mass energy. The thermal energy is dominated by radiation and can be released at the photospheric radius  $R_*$  where the jet becomes transparent. For sufficiently clean (baryon-poor) thermal jets, transparency occurs when radiation still carries most of the explosion energy. Such a “radiation-dominated” GRB has a high radiative efficiency and a spectrum that peaks near 1 MeV (Paczynski 1986; Goodman 1986). The shape of the spectrum in this case should be Planckian (Beloborodov 2011, hereafter B11).

The observed emission indeed peaks near 1 MeV in most bursts, however its spectrum is nonthermal, with an extended tail of high-energy emission. This has two implications: (1) the GRB photosphere is rarely radiation-dominated, and (2) some form of dissipation operates in the GRB jets and greatly broadens their radiation spectra. The free energy available for dissipation may be kinetic or magnetic. In particular, the relative motion of different parts of the jet can be dissipated (e.g. Rees & Meszaros 1994; Paczynski & Xu 1994). It leads to collisionless shocks as well as collisional dissipation.

Collisionless shocks are known as efficient accelerators of nonthermal particles in astrophysics. They offer a mechanism for generating nonthermal electrons in GRB jets, and their synchrotron emission may be associated with observed  $\gamma$ -rays. The idea became popular, however it faces difficulties. First, recent *ab initio* particle-in-cell simulations of collisionless shocks (e.g. Sironi & Spitkovsky 2009, 2011) do not support this scenario. The nonthermal electron accel-

eration by shocks should be inefficient in GRB jets with expected transverse magnetic fields and magnetization parameter  $\varepsilon_B > 10^{-3}$ . Secondly, the spectra of a large number of GRBs observed by *CGRO*/BATSE and *Fermi*/GBM instruments are inconsistent with synchrotron emission, especially in the fast-cooling regime that is expected in the model (e.g. Preece et al. 2000). Some of the spectra show harder slopes than synchrotron emission can produce irrespective of the cooling regime. In addition, the synchrotron model does not predict the observed preferential peak of the spectra near 1 MeV. A recent discussion of the internal-shock synchrotron model can be found in Daigne et al. (2011).

One can consider different phenomenological models of emission from the optically thin region of the jet at  $r > R_*$ . One proposed model associates the prompt GRB with synchrotron self-Compton radiation from continually and uniformly heated plasma (Stern & Poutanen 2004; Vurm & Poutanen 2009). The optically thin plasma maintains a relativistic temperature,  $kT_e \gg m_e c^2$ , at which radiative cooling balances the heating, and keeps radiating as the jet expands. While this model can produce hard spectra, it still does not explain the preferential position of the observed spectrum peak. It also conflicts with the recently observed high-energy spectra of GRBs (e.g. Abdo et al. 2009b; Zhang et al. 2011).

A likely resolution of these problems is that the bulk of GRB luminosity is generated at small radii  $r \lesssim R_*$  rather than in the optically thin zone  $r > R_*$ . Then multiple Compton scattering participates in the spectrum formation and can naturally produce the observed spectra. Generally, any sub-photospheric heating leads to Comptonization of the (initially thermal) photons, and then radiation released at the photosphere  $R_*$  looks as nonthermal while the peak of its spectrum remains near 1 MeV (Thompson 1994; Mészáros & Rees 2000b; Pe’er et al. 2006; Giannios 2006; Pe’er et al. 2006; Beloborodov 2010, hereafter B10). A variety of Comptonized spectra may be generated, depending on the assumptions of

the model. Further progress can only be made when the physical mechanism of energy dissipation is understood. It could be thermal or nonthermal, and its radial dependence is important for the emerging spectrum.

Three heating mechanisms can operate in the subphotospheric region. Two of them (internal shocks and magnetic dissipation) rely on collisionless plasma processes, whose details remain uncertain because of their great complexity. The third mechanism (collisional heating) is straightforward and can be modeled from first principles. It was recently proposed that collisional heating shapes the GRB spectra (B10). It will be the focus of the present paper.

Collisional heating is particularly strong (and inevitable) in jets that carry free neutrons (Derishev et al. 1999; Bahcall & Mészáros 2000; Fuller et al. 2000; Mészáros & Rees 2000a; Rossi et al. 2006; Koers & Giannios 2007). It is discussed in some detail in Section 2 below. Before the complete decoupling of neutrons and protons into two non-interacting components, the fading  $n$ - $p$  collisions heat the protons to a mildly relativistic temperature. Importantly, the  $n$ - $p$  collisions also create  $e^\pm$  plasma that efficiently radiates its energy. This plasma is cooled by the radiative losses and heated by Coulomb collisions with hot protons. The rates of all these processes are well known and their effect on the jet and radiation can be calculated without additional assumptions (B10). In particular, one can show that the electron distribution function has two parts, thermal and nonthermal, and both Comptonize the radiation carried by the jet.

Three features of collisional heating make it a promising emission mechanism: (1) It peaks at radii  $r \sim 0.1R_*$ , not too early and not too late to produce a bright photospheric emission. (2) It has a high radiative efficiency, comparable to 50%. (3) The radiation spectrum produced by collisional heating can be accurately calculated from first principles. The striking result reported in B10 is that the spectrum has the Band-type shape with the high-energy photon index  $\beta \sim -2.5$ , which is consistent with observations.

The formation of radiation spectrum in a heated jet is a non-linear problem that requires a self-consistent calculation of the plasma and radiation behavior. This problem was solved in B10 using a Monte-Carlo radiative transfer code in combination with an iterative technique. In the present work we use a different method. Our paper has two goals:

First, to provide an independent check of the result of B10, we calculate the emitted spectrum using a completely different method: we solve the kinetic equations for the plasma and radiation in the jet. We use the numerical code described in Vurm & Poutanen (2009, hereafter VP09). We develop a new version of the code to adapt it to GRB jets, calculate the emerging radiation spectrum, and compare the results with those of B10.

Secondly, the numerical models in B10 were limited to weakly magnetized flows,  $\varepsilon_B \ll 1$ , and neglected synchrotron emission. In the present paper, we explore the spectra produced by magnetized neutron-loaded jets for a range of  $0 < \varepsilon_B < 2$  and include synchrotron emission and self-absorption.

The paper is organized as follows. Section 2 describes the physical model and the setup of the simulations. Section 3 describes our method of calculations. The results are presented in Sections 4 and 5 and discussed in Section 6.

## 2. PHYSICAL MODEL AND SIMULATION SETUP

The central engines of GRBs must be compact and hot objects, which are almost certainly neutron rich. The high density and temperature inevitably leads to  $\beta$ -equilibrium (Imshennik et al. 1967; Derishev et al. 1999; Beloborodov 2003). For all plausible parameters of the central engine, the equilibrium establishes a high fraction of free neutrons in the baryonic matter (this feature is seen, for example, in the accretion-disk model for GRBs, see Beloborodov 2008 for a review). Therefore, neutrons are generally expected in GRB jets.

The presence of neutrons creates perfect conditions for strong collisional heating. In any variable baryonic jet, the inter-penetrating neutron and proton components inevitably develop relative motions (see B10 and references therein). The two components acquire different Lorentz factors  $\Gamma_n$  and  $\Gamma$ , and (rare) collisions between neutrons and protons dissipate enormous energy. The dissipation is strongest in those parts of the jet where  $\Gamma/\Gamma_n$  is highest.

The variable jet consists of many causally disconnected shells. Different shells are accelerated to different Lorentz factors and emit different radiation, which is consistent with observed variability. In our simulations, we focus on the heating history and radiation of one shell. The shell is launched from the central source and accelerated at the expense of its internal energy until it enters the coasting matter-dominated phase of expansion. At radius  $R_n$ , the timescale for collisions between the neutron and proton components exceeds the expansion timescale of the jet, and protons start to migrate relative to neutrons, forming a compound flow with  $\Gamma \neq \Gamma_n$ . At this point, strong collisional heating begins and the radiation spectrum starts deviating from a blackbody. Our simulation starts at  $R_n$  and follows this evolution. We assume that  $\Gamma$  and  $\Gamma_n$  remain approximately constant till the end of the simulation (see B10 for discussion of this approximation).

$R_n$  may be defined as the radius where the neutron flow becomes “optically thin” to collisions with protons. The corresponding “optical depth” for this process at radius  $r$  is given by

$$\tau_n = \frac{n_n \sigma_n r}{\Gamma_n} = \frac{L_n \sigma_n}{4\pi m_n c^3 r \Gamma_n^3} = \frac{R_n}{r}, \quad (1)$$

where  $n_n$  is the comoving number density of the neutron flow,  $L_n = 4\pi m_n c^3 r^2 \Gamma_n^2 n_n$  is its kinetic luminosity (isotropic equivalent) and  $\sigma_n \sim 3 \times 10^{-26} \text{ cm}^2$  is the effective cross-section for nuclear collisions. Radius  $R_n$  is defined so that  $\tau_n(R_n) = 1$ ,

$$R_n = \frac{L_n \sigma_n}{4\pi m_n c^3 \Gamma_n^3}. \quad (2)$$

We aim to calculate the evolution of electron/positron and photon distribution functions in the heated jet. The photon spectrum is controlled by electrons (and positrons) via Compton scattering and synchrotron emission. Therefore, the key ingredient of any GRB model is how energy is injected into electrons. For the model studied in this paper, the electron heating is unambiguously determined by the collisional processes as described below (see B10 for detailed discussion).

The electron heating comes from baryons, in two forms.

1. Nuclear  $n$ - $p$  collisions generate  $e^\pm$  pairs whose energy in the comoving frame of the jet is comparable to the

pion rest-mass,  $\gamma m_e c^2 \sim m_\pi c^2 \approx 140$  MeV. The injection rate of these energetic particles is proportional to the rate of nuclear collisions,  $\dot{n}_{\text{coll}} = c\sigma_n n n_n \Gamma_{\text{rel}}$ , where  $\Gamma_{\text{rel}} \approx \frac{1}{2}(\Gamma/\Gamma_n + \Gamma_n/\Gamma)$  is the relative Lorentz factor of collisions. The  $e^\pm$  injection rate is given by (B10),

$$\dot{n}_\pm^{\text{inj}} \approx \frac{1}{4} \frac{\Gamma_{\text{rel}} m_p}{\gamma_0 m_e} \dot{n}_{\text{coll}} \approx \frac{3}{8} \frac{\Gamma}{\Gamma_n} \tau_n \frac{n}{t_{\text{exp}}}. \quad (3)$$

Here  $n$  is the proton number density in the plasma rest frame and

$$t_{\text{exp}} \equiv \frac{r}{c\Gamma} \quad (4)$$

is the expansion timescale of the plasma, measured in its rest frame. The  $e^\pm$  injection peaks near the Lorentz factor  $\gamma_0 \approx m_\pi/m_e \approx 300$ . We will approximate it by a Gaussian distribution centered at  $\gamma_0 = 300$ . These energetic particles experience rapid radiative cooling and join the thermal  $e^\pm$  population.

2. The  $e^\pm$  population receives energy from protons via Coulomb collisions. Note that protons have at least mildly relativistic random velocities — they are stirred by  $n$ - $p$  collisions. The dominant majority of  $e^\pm$  pairs are kept at a much lower temperature, because of Compton cooling. Coulomb collisions drain the energy from protons to  $e^\pm$  with the following rate (e.g. Ginzburg & Syrovatskii 1964)

$$\dot{Q}_{\text{th}} = \frac{3}{2} \ln \Lambda \frac{\sigma_T m_e c^3 n_e n}{\beta_p} \approx 0.02 \tau_T \frac{nm_p c^2}{t_{\text{exp}}}, \quad (5)$$

where  $\ln \Lambda$  is the Coulomb logarithm,  $\beta_p \sim 1$  is the random velocity of the protons stirred by nuclear collisions,  $n_e = n_- + n_+$  is the number density of electrons and positrons, and

$$\tau_T = \frac{n_e \sigma_T r}{\Gamma} \quad (6)$$

is a characteristic Thomson optical depth of the plasma, as seen by photons at radius  $r$ . The pair density  $n_e$  is controlled by the process of  $e^\pm$  injection (Equation 3), the subsequent pair-photon cascade in the radiation field, and  $e^\pm$  annihilation, all of which must be self-consistently calculated.

Equations (3) and (5) determine the heating history of the expanding plasma shell and eventually the radiation spectrum emitted by this shell. The shell itself is a part of the (variable) jet. It has the following parameters:

1. Lorentz factor and kinetic luminosity ( $\Gamma$  and  $L$  for the plasma component and  $\Gamma_n$  and  $L_n$  for the neutron component; it is reasonable to expect that  $L_n$  is roughly proportional to  $L$ ). Note that the characteristic radius  $R_n$  for a given shell is determined by its  $\Gamma_n$  and  $L_n$  according to Equation (2).
2. Temperature of the thermal radiation at  $R_n$ , prior to the onset of collisional heating,  $T_{\text{BB}}(R_n)$ . The corresponding luminosity is  $L_{\text{BB}} = (4/3) c a T_{\text{BB}}^4 \Gamma^2 4\pi R_n^2$  (here  $a$  is the radiation density constant). This parameter depends on  $L$ ,  $\Gamma$ , and the radius at the base of the jet  $r_0$  where our shell starts to accelerate. We fix  $r_0 = 10^7$  cm

in our numerical models and calculate the corresponding  $T_{\text{BB}}(R_n)$  using the standard model of adiabatically cooled outflow between  $r_0$  and  $R_n$  (see e.g. Paczynski 1990; Piran et al. 1993).

3. Magnetization  $\varepsilon_B$ . It is defined as the ratio of the magnetic energy density  $U_B = B^2/8\pi$  to the proper energy density of the plasma flow  $U = L/4\pi cr^2 \Gamma^2$  (which includes rest-mass energy). Both  $U_B$  and  $U$  are measured in the comoving frame of the plasma. We assume that the magnetic field is advected from the central engine. Then the field must be transverse to the (radial) velocity<sup>1</sup> and scale with radius as  $B \propto r^{-1}$ . In this case  $\varepsilon_B = U_B/U \approx \text{const}$ , i.e. does not change with radius.

### 3. METHOD OF CALCULATIONS

For our calculations we use a new version of the numerical code developed by VP09. The code is designed to model the coupled evolution of the heated outflow and the radiation it carries. The evolution is tracked by solving the time-dependent kinetic equations for the particles and photons. The included interactions are Compton scattering, cyclo-synchrotron emission and absorption, photon-photon pair production and annihilation, and Coulomb collisions. We use the exact cross-sections or rates for all these processes.

The original version of the code had one significant limitation: it used the “one-zone” or “leaking-box” approximation. This approximation pictures a uniform plasma cloud of an optical depth  $\tau_T$  with isotropic populations of particles and photons. It treats the loss of photons from the cloud using an escape probability instead of accurate calculations of radiation diffusion through the cloud (VP09).

The leaking-box picture is not good for GRB jets. In contrast to static sources, where radiation escapes the source on timescale  $\sim \tau_T R/c$ , GRB radiation remains embedded in the relativistic jet at all radii of interest. It evolves with radius according to the radiative transfer equation, which is in serious conflict with the one-zone approximation. For example, the true angular distribution of radiation in the jet comoving frame is far from being isotropic, even in the subphotospheric region (B11). The isotropic approximation of the one-zone model becomes invalid when the optical depth  $\tau_T$  decreases below  $\sim 10$ . Furthermore, the large free path of photons near the photosphere leads to mixing of radiation emitted by different parts of the photospheric region with different Doppler shifts. This mixing has a significant effect on the local photon spectrum and the spectrum received by a distant observer.

For these reasons the simplified one-zone treatment has to be abandoned in favor of proper radiative transfer calculations. The kinetic equation for photons in VP09 is replaced by the transfer equation.

#### 3.1. Radiative transfer

The equation of radiative transfer in an ultra-relativistic, matter-dominated outflow reads (B11)

$$\frac{\partial I_\nu}{\partial \ln r} = (1 - \mu) \left( \frac{\partial I_\nu}{\partial \ln \nu} - 3I_\nu \right) - (1 - \mu^2) \frac{\partial I_\nu}{\partial \mu} + \frac{r(j_\nu - \kappa_\nu I_\nu)}{\Gamma(1 + \mu)}. \quad (7)$$

<sup>1</sup> The radial component  $B_r$  is suppressed as  $r^{-2}$  in the expanding plasma and can be neglected.

Here  $I_\nu$  is the specific intensity,  $\nu$  is the photon frequency,  $\mu = \cos \theta$ ,  $\theta$  is the angle relative to the radial direction, and  $r$  is the distance from the central source. The emission and absorption coefficients  $j_\nu$  and  $\kappa_\nu$  represent all the interactions of radiation with plasma as well as with radiation itself. All quantities (except  $r$  and  $\Gamma$ ) are measured in the rest frame of the outflow.

Equation (7) and the formulation of the ultra-relativistic transfer problem are discussed in detail in B11. The problem simplifies because essentially all photons flow toward larger  $r$ , and hence only inner boundary conditions need to be specified. The radiative transfer then takes the form of an initial-value problem. One can think of it as the evolution of  $I_\nu$  with  $r$  or, equivalently, with the jet comoving time  $t$ . Equation (7) is similar to the kinetic equation for the evolution of the photon distribution function (VP09), with additional terms due to the angular dependence.

The inner boundary condition for  $I_\nu$  is the blackbody radiation of a given temperature. We track the evolution of radiation with  $r$  consistently with the plasma evolution, which is described in Section 3.2. In the case of a passively cooling jet (no heating), the transfer equation reproduces the adiabatic cooling of photons in the subphotospheric region. Heating changes the state of the plasma and greatly affects the source function  $S_\nu = j_\nu/\kappa_\nu$  that governs the radiative transfer.

Our numerical solution of Equation (7) will use one approximation to reduce the computational time: when calculating  $j_\nu$  and  $\kappa_\nu$  we pretend that radiation is isotropic, using only the zeroth moment of the actual angular distribution of photons. In particular, the scattering rates are averaged over angles. The approximation is known to be quite successful in classical transfer problems (e.g. Chandrasekhar 1960). It is also reasonable for GRB outflows if the bulk of scattering events are non-relativistic in the plasma rest frame (B11). Its error becomes more significant at high photon energies, comparable to  $m_e c^2$  in the plasma frame. This approximation allows us to use the numerical tools for  $j_\nu$  and  $\kappa_\nu$  developed in VP09. A detailed discussion of the angle-averaged  $j_\nu$  and  $\kappa_\nu$  and their numerical treatment is found in that work.

Radiation that will be received by a distant observer is determined by  $I_\nu$  at a large enough radius, where photons stream almost freely at all relevant  $\nu$  (note that this radius is much larger than  $R_*$ , as will be discussed below). Using  $1 - \Gamma^{-2} \approx 1$ , we define Doppler factor as  $\mathcal{D} = \Gamma(1 + \mu)$ . The spectral distribution of the observed (isotropic equivalent) luminosity  $L_\gamma$  is given by the Lorentz transformation to the observer frame and integration over angles,

$$L_\gamma(E) \equiv dL_\gamma/dE = \frac{8\pi^2}{h} R^2 \int_{-1}^1 I_\nu(\mu) \mathcal{D}(\mu) d\mu, \quad (8)$$

where  $E = Dh\nu$  is the observed photon energy and  $h$  is the Planck constant. We emphasize that the simple relation (8) is valid only at large radii, after all transfer effects on  $I_\nu$  have been calculated according to Equation (7).

Finally, we note that Equation (7) was formally derived for steady outflows, however it is also applicable to strongly variable, non-uniform jets (see B11 and Appendix A). The basic reason for this is that radiation moves together with the ultra-relativistic plasma flow. The photon diffusion in the plasma rest frame is limited to scales  $\delta \sim ct \sim r/\Gamma$ , which are much smaller than  $r$ . When viewed in the fixed observer frame, the scale of diffusion in the radial direction is additionally compressed by the factor of  $\Gamma^{-1}$ . The transfer occurs in a thin

shell (or ‘‘pancake’’) of the jet as if it were part of a steady outflow.

### 3.2. Kinetic equation for plasma

The comoving-frame kinetic equation for electrons and positrons can be written as

$$\begin{aligned} \frac{\partial n_\pm(p)}{\partial t} = & -\frac{\partial}{\partial p} \left[ \dot{p} n_\pm(p) - \frac{1}{2} \frac{\partial}{\partial \gamma} (D n_\pm(p)) \right] \\ & + j_\pm - \kappa_\pm n_\pm(p) - \frac{2}{t} n_\pm(p). \end{aligned} \quad (9)$$

Here  $p = \sqrt{\gamma^2 - 1}$  is the electron/positron momentum in units of  $m_e c$ ,  $n_\pm(p)$  are the distribution functions of positrons and electrons, and  $t = r/c\Gamma$  is the proper time of the flow. When calculating  $\dot{p}$  we take into account Coulomb heating by protons (Equation 5) and adiabatic cooling (Equation 10 below). The term  $\dot{p}$  also includes the usual contributions from Compton scattering (in the Thomson regime), synchrotron emission and self-absorption, and Coulomb collisions between  $e^\pm$ , as described in VP09. The diffusion coefficient  $D$  governs particle thermalization at low energies due to synchrotron processes and Coulomb collisions between  $e^\pm$  (VP09). The source  $j_\pm$  includes the injection of high-energy pairs by inelastic nuclear collisions as described in Section 2. The source and sink terms  $j_\pm$  and  $\kappa_\pm$  also contain contributions from photon-photon pair production, pair annihilation, and Compton scattering (in the Klein-Nishina regime). Our code calculates all these processes using the exact cross-sections, as described in detail in VP09. Finally, the last term in Equation (9) takes into account the dilution of particle densities due to the two-dimensional (sideways) expansion of the coasting flow.

The contribution of adiabatic cooling to  $\dot{p}$  is given by

$$\dot{p}_{\text{ad}} = -\frac{2}{3} \frac{p}{t}. \quad (10)$$

This is easy to verify by considering adiabatic expansion of  $\mathcal{N}_e$  monoenergetic electrons occupying a volume  $V$ . Their pressure  $P_e = (\mathcal{N}_e/V)(p^2/3\gamma)m_e c^2$  determines the adiabatic cooling rate  $\mathcal{N}_e m_e c^2 d\gamma = -P_e dV$ . The coasting outflow expands in two dimensions,  $V \propto r^2 \propto t^2$ . Using  $dp = (\gamma/p)d\gamma$ , one gets Equation (10).

In our numerical simulations, the electron/positron kinetic equation (9) is discretized on a grid of particle momenta and solved simultaneously with the radiative transfer equation (7). The grid of dimensionless momentum  $p$  extends from  $10^{-4}$  to  $10^4$ , with 25 points per decade. The photon-energy grid spans 15 decades from  $h\nu/m_e c^2 = 10^{-11}$  to  $10^4$  (comoving frame), with approximately 13 gridpoints per decade. The lower boundary is set so low to properly simulate the effects of synchrotron self-absorption in mildly relativistic pairs in a weak magnetic field. The photon angular grid is uniform in  $\theta$  and has 40 grid points.

## 4. NON-MAGNETIZED OUTFLOWS

We begin with the non-magnetized model that can be directly compared with the results in B10. The model has the following parameters: proton flow luminosity  $L = 10^{52}$  erg  $s^{-1}$ , neutron flow luminosity  $L_n = 2 \times 10^{51}$  erg  $s^{-1}$ , Lorentz factor of the proton flow (baryon loading)  $\Gamma = 600$ , Lorentz factor of the neutron flow  $\Gamma_n = 100$ , initial radius of the flow  $r_0 = 10^7$  cm. The starting radius of the simulations is determined by Equation (2), which gives  $R_n = 10^{11}$  cm. The

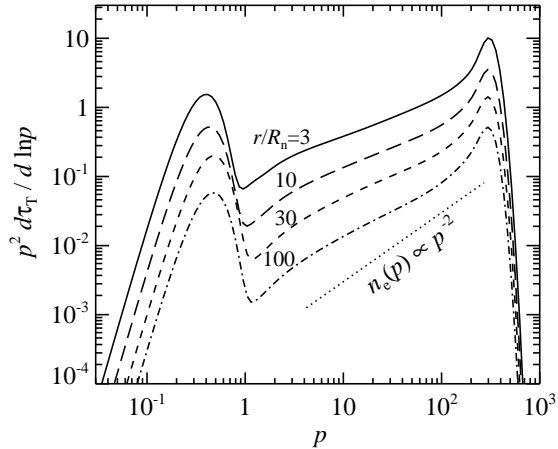


**Figure 1.** Momentum distribution function for electrons and positrons in the non-magnetized jet at different radii:  $r/R_n = 3, 10, 30,$  and  $100$  (solid, long-dashed, dashed and dot-dashed curves, respectively). The distribution is normalized so that it shows the optical depth  $\tau_T$ , which is related to density  $n_e = n_+ + n_-$  by Equation (6). The dotted line indicates the slope of a nonthermal distribution that would be obtained if the injected  $e^\pm$  did not produce a cascade and were Compton-cooled in the Thomson regime.

comoving temperature of the blackbody radiation field at  $R_n$  is found from the passively cooling outflow model at  $r < R_n$ , which gives  $kT_{\text{BB}}(R_n) \approx 0.5$  keV.

#### 4.1. Electron/positron distribution

At the radius  $R_n$ , where the dissipation begins, the injected high-energy pairs start to upscatter the thermal photons to energies up to  $\sim 100m_e c^2$  in the rest-frame of the jet. The optical depth for photon-photon pair production seen by the high-energy photons is initially small, as the radiation spectrum is dominated by the blackbody component that is below the threshold for photon-photon pair production reaction. However, this soon changes as more and more photons are upscattered from the thermal distribution. Then the jet becomes optically thick to pair production and a cascade develops. Soon the annihilation balance is established, in which the cooled  $e^\pm$  pairs annihilate at the same rate as the new pairs are created by the cascade.

The continual cascade quickly reaches a steady state, on a timescale shorter than the jet expansion timescale. Then a quasi-steady  $e^\pm$  distribution is maintained, which gradually changes with radius (Figure 1). The distribution has two parts, thermal and nonthermal (see B10). The nonthermal tail consists of continually injected, fast-cooling  $e^\pm$  pairs. If the injected  $e^\pm$  generated no cascade and cooled in Thomson regime at all  $p$ , the nonthermal tail would have a power-law form  $n_e(p) \propto p^{-2}$ . The actual distribution is affected by the Klein-Nishina effects in Compton cooling (which are significant at  $p > 50$ ) and the large number of secondary pairs produced in the cascade.

The low-energy peak of the  $e^\pm$  distribution maintains a Maxwellian shape due to Coulomb collisions between  $e^\pm$  particles. This thermalized population is continually heated by Coulomb collisions with protons and maintains the equilibrium temperature that is determined by the balance between Coulomb heating and Compton cooling. The resulting electron temperature is close to 15 keV and remarkably stable throughout the dissipation region (see Figure 4 below). Its (weak) radial dependence is approximately described by equation (32) in B10.

Shortly after the dissipation starts, the scattering opacity of

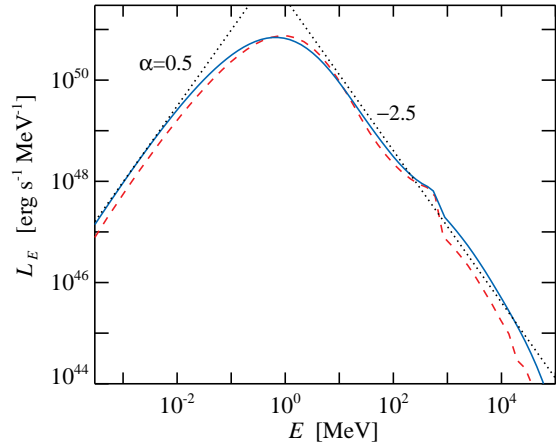


**Figure 2.** Comparison of spectra obtained by kinetic (solid line) and Monte Carlo (dashed line) simulations for the non-magnetized jet. Model parameters: proton flow luminosity  $L = 10^{52}$  erg  $s^{-1}$ , neutron flow luminosity  $L_n = 2 \times 10^{51}$  erg  $s^{-1}$ , Lorentz factor of the proton flow  $\Gamma = 600$ , Lorentz factor of the neutron flow  $\Gamma_n = 100$ . The dotted straight lines correspond to photon indices 0.5 and  $-2.5$ .

the flow becomes dominated by the created  $e^\pm$  pairs. The Thomson optical depth is regulated to  $\tau_T \approx 20$  near  $R_n$  and then decreases as  $R_n/r$  (see Figure 1), in excellent agreement with B10. This places the photospheric radius at  $R_* \sim 20R_n$ .

Since  $\tau_T \propto n_e r \propto r^{-1}$ , Equation (5) shows that the Coulomb heating peaks near  $R_n$ , and the fraction of the flow energy dissipated in one dynamical time at larger radii scales as  $r^{-1}$ . The nonthermal energy injection has the same  $r^{-1}$  dependence. Thus, the ratio of thermal and nonthermal heating rates remains nearly constant along the flow. This ratio is close to unity.

Most of the kinetic energy of the flow is dissipated (and re-dissipated) by collisional heating. One should keep in mind though that the heat given to plasma and radiation in the sub-photospheric region is continually degraded by adiabatic cooling. As a result, the actual luminosity released at the photosphere is smaller by a factor of 1/2 compared with the total heat deposited in the flow (see section 4.6 in B10).

#### 4.2. Radiation spectrum

The spectrum that should be received by a distant observer from the collisionally heated jet is shown in Figure 2. For comparison, we also show the result of the Monte-Carlo simulation in B10. The two spectra are very similar.

The emitted spectrum peaks near 1 MeV. Radiation below the peak is made of blackbody photons advected from the central source and released at the photosphere. Note that the low-energy photon index  $\alpha \approx 0.4 - 0.5$  is significantly different from the Rayleigh-Jeans  $\alpha = 1$ . This softening is a result of the superposition of emissions from different parts of the photosphere having different Doppler factors, i.e. effectively a multi-temperature spectrum is observed below the peak (B10). The spectrum between 1 and 20 MeV is mainly shaped by thermal Comptonization by Coulomb-heated pairs. The thermal pairs upscatter photons to energies up to  $E \sim 2\Gamma kT_e \sim 20$  MeV in the observed frame, where  $kT_e \sim 15$  keV is the electron temperature in the comoving frame.

Above 20 MeV, the inverse Compton scattering by nonthermal pairs dominates the observed spectrum. Note that there is no dip between the thermal and nonthermal components. Two reasons contribute to this remarkable smoothness of the

spectral shape. First, the energy budgets of thermal and non-thermal Comptonization are comparable, and the two components have comparable luminosities at 10–20 MeV. Secondly, most of the photons above 20 MeV undergo several scattering events on thermal pairs before escaping. They experience significant Compton downscattering, which has an overall smoothing effect on the spectrum. The only distinct feature of the predicted high-energy spectrum is a broad annihilation line on top of the smooth continuum just below 1 GeV, from cooled  $e^\pm$  pairs. Photon energy  $E \sim 1$  GeV in the observer frame approximately corresponds to  $h\nu \sim m_e c^2$  in the jet frame.

The observed spectrum at energies  $E > 1$  GeV is affected by absorption due to photon-photon ( $\gamma$ - $\gamma$ ) pair production. The jet is optically thick to GeV photons close to  $R_n$  where most of the heating occurs, and all high-energy upscattered photons are quickly absorbed, creating secondary  $e^\pm$  pairs. Thus, the developing pair-photon cascade is initially in the saturated regime.

The photon emissivity  $j_\nu$  produced by the saturated cascade may be estimated analytically (Svensson 1987). An important parameter of the cascade is  $z_T = (2/3)\gamma_0 x_0$ , where  $\gamma_0$  is the injection Lorentz factor of the primary nonthermal pairs and  $x_0 = h\nu_0/m_e c^2$  is the typical energy of soft photons. The quantity  $z_T$  determines whether the cascade takes place in the Thomson or Klein-Nishina regime ( $z_T \leq 0.5$  or  $> 0.5$ , respectively), the number of generations of secondary pairs etc. In our case  $x_0 \sim 1/200$  and  $\gamma_0 = 300$ , so  $z_T \sim 1$ , i.e. the cascade starts in the Klein-Nishina regime at high energies and proceeds in the Thomson regime at lower energies. There are several generations of secondary pairs and photons, leading to a smooth overall spectrum. For the cascade with  $z_T \sim 1$  the analytic solution predicts a flat emissivity of high-energy photons,  $\nu j_\nu \approx \text{const}$  (Svensson 1987). The radiation intensity inside an opaque source is given by  $I_\nu = j_\nu/\kappa_{\nu,\gamma\gamma}$ . Here the absorption coefficient  $\kappa_{\nu,\gamma\gamma} \propto \nu^{-\beta-1}$  and  $\beta$  is the photon index of the target radiation (typically photons of multi-MeV energy in the observer frame). Thus, the high-energy spectrum  $I_\nu \propto \nu^\beta$  is maintained inside the opaque jet.

The escaping multi-GeV emission may be estimated by considering the evolution of  $\gamma$ - $\gamma$  opacity with radius (B10). The rate of nuclear collisions fades at large radii, but it still generates a significant  $e^\pm$  cascade. Since the  $\gamma$ - $\gamma$  optical depth decreases with  $r$ , the multi-GeV photons produced in the outer region have a chance to escape. The radius of  $\gamma$ - $\gamma$  transparency at energy  $E$  scales approximately as  $R_{\gamma\gamma} \propto E^{-\beta-1}$ , and the power of the cascade scales as  $r^{-1}$ . This leads to  $L_\gamma(E) \propto E^\beta$  (photon index  $\beta - 1$ ). This rough estimate suggests the change in photon index above a few GeV from  $\beta$  to  $\beta - 1$ . A similar steepening of the spectrum is observed in Figure 2.<sup>2</sup> Note that the high-energy radiation escaping from the collisionally heated jet extends far beyond 1 GeV, up to 100 GeV.

Finally, note that our spectrum somewhat deviates from that of B10 in the GeV range. This is likely caused by our angle-averaged approximation for  $j_\nu$  and  $\kappa_\nu$  (Section 3.1). Anisotropy effects are particularly significant at the high-energy end of the spectrum that forms at large radii. At  $r \gg R_*$  the soft photon field is strongly collimated, and the

<sup>2</sup> Incidentally, the high-energy radiation inside the opaque source  $I_\nu = j_\nu/\kappa_{\nu,\gamma\gamma}$  also has the photon index  $\beta - 1$ . This coincidence is a result of the particular scaling  $j_\nu \propto r^{-4}$  and  $\kappa_{\nu,\gamma\gamma} \propto r^{-2}$  in the collisionally heated jet.

**Table 1**  
Results of simulations.

$\varepsilon_B^a$	$E_{\text{peak}}^b$ (MeV)	$\alpha^c$	$\varepsilon_{\text{rad}}^d$	$R_*/R_n^e$	$Y^f$	$\dot{Q}_{\text{th}}/\dot{Q}_{\text{nth}}^g$	$kT_e^h$ (keV)
0	2.9	-0.6	0.46	16.5	0.19	0.94	15.0
$10^{-3}$	2.5	-0.8	0.46	16.1	0.18	0.92	14.7
$10^{-2}$	1.7	-1.2	0.45	14.2	0.14	0.79	13.8
0.1	1.2	-1.4	0.46	8.8	0.058	0.32	13.1
0.5	1.3	-1.4	0.52	2.3	0.014	0.10	13.1
2.0	1.4	-1.3	0.55	0.5	0.005	0.05	14.4

<sup>a</sup>Magnetization.

<sup>b</sup>Peak energy of the  $EL_E$  spectrum.

<sup>c</sup>Photon index in the 100–500 keV range.

<sup>d</sup>Radiative efficiency  $\varepsilon_{\text{rad}} = L_\gamma/L$ .

<sup>e</sup>Radius of the Thomson photosphere relative to the radius  $R_n = 10^{11}$  cm where the dissipation starts. In the case of  $\varepsilon_B = 2$ , the jet remains optically thin throughout the collisionally heated region.

<sup>f</sup>Pair yield  $Y = \mathcal{M}/\gamma_0$ , where  $\mathcal{M}$  is the secondary pair multiplicity and  $\gamma_0 = 300$  is the Lorentz factor of injected electrons.

<sup>g</sup>Ratio of thermal and nonthermal heating rates at  $R_*/5$  for cases with  $\varepsilon_B \leq 10^{-2}$ , and at the radius of maximal optical depth for cases with  $\varepsilon_B \geq 0.1$ .

<sup>h</sup>Pair temperature at  $R_*/5$  for  $\varepsilon_B \leq 10^{-2}$ , and at maximal optical depth for  $\varepsilon_B \geq 0.1$ .

scattering of nearly radial photons by relativistic pairs is preferentially backward. The backward-scattered photons see a higher  $\gamma$ - $\gamma$  optical depth and less of them can get out. The anisotropy of  $\gamma$ - $\gamma$  opacity is further enhanced by the very same collimation of the soft radiation field. These effects create particularly strong angular dependence of  $j_\nu$  and  $\kappa_\nu$  at high energies, which is missed by our approximation.

## 5. MAGNETIZED OUTFLOWS

Magnetization of the jet is described by the parameter

$$\varepsilon_B = \frac{4\pi r^2 c \Gamma^2 U_B}{L}, \quad (11)$$

where  $U_B = B^2/8\pi$  is the magnetic energy measured in the rest frame of the outflowing plasma. The quantity  $\varepsilon_B$  is the ratio of the Poynting flux (measured in the static frame) to the kinetic luminosity of the outflow  $L$ . Let us consider the GRB model with the same parameters as in Section 4 and investigate how the results change if the jet is magnetized, i.e.  $\varepsilon_B \neq 0$ . We have calculated a set of models with  $\varepsilon_B = 10^{-3}$ ,  $10^{-2}$ , 0.1, 0.5 and 2. The corresponding ratios of (comoving) magnetic and radiation energy densities at the start of simulations are  $U_B(R_n)/U_\gamma(R_n) = 0.006, 0.06, 0.6, 3$  and 12. The results of our calculations are summarized in Table 1 and described in detail below.

### 5.1. Electron/positron distribution

Strong magnetic fields imply significant synchrotron cooling of the high-energy  $e^\pm$  pairs injected by nuclear collisions, which can compete with Compton cooling. Since the synchrotron photons do not create secondary pairs, the magnetic field has a suppressing effect on the  $e^\pm$  cascade. One can show that the multiplicity of each subsequent pair generation in a saturated cascade is suppressed by the factor  $f_B \approx 1 + \varepsilon_B/\varepsilon_{\text{rad}}$ , where  $\varepsilon_{\text{rad}} = L_\gamma/L$  is the fraction of the jet energy carried by radiation. For magnetic fields approaching equipartition with radiation (i.e.  $\varepsilon_B L/L_\gamma \sim 1$ ), only two generations of secondary pairs can make a significant contribution to the total pair multiplicity.

As a result, the total pair yield decreases from  $Y \approx 0.2$  into about 0.005 as  $\varepsilon_B$  increases from 0 to 2 (Table 1). The pair

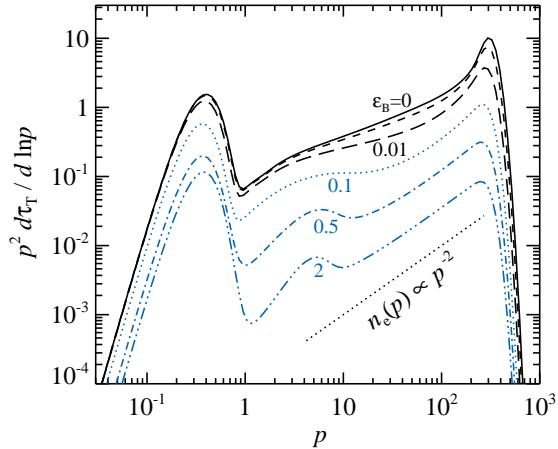


**Figure 3.** Momentum distribution of electrons and positrons at radius  $r/R_n = 3$  in the magnetized jet. The jet parameters are the same as in Figures 1 and 2 except for magnetization. Different curves show models with different  $\varepsilon_B$ :  $\varepsilon_B = 0$  (solid),  $10^{-3}$  (short-dashed), 0.01 (long-dashed), 0.1 (dotted), 0.5 (dot-dashed) and 2 (triple-dot-dashed). The bump near  $p \sim 5$  is the result of synchrotron self-absorption, which becomes increasingly important at high  $\varepsilon_B$ . The dotted line indicates the slope of a nonthermal distribution that would be obtained if the injected  $e^\pm$  lost energy only by emitting synchrotron radiation, with no inverse-Compton  $e^\pm$  cascade and no self-absorption of synchrotron radiation.

yield is defined as  $Y = \mathcal{M}/\gamma_0$ , where  $\mathcal{M}$  is the multiplicity of secondary pairs. In the model with  $\varepsilon_B = 2$ , the pair yield is not far from the minimum value  $Y = 1/\gamma_0$ , which corresponds to  $\mathcal{M} = 1$  (no secondary pairs). The strong field completely suppresses the cascade.

Figure 3 shows the  $e^\pm$  distribution function at  $r = 3R_n$ . The overall shape of the distribution is similar to that found in non-magnetized jets. It has thermal and nonthermal parts. With increasing  $\varepsilon_B$ , the normalization of the distribution significantly decreases — the number of  $e^\pm$  is reduced as the cascade is suppressed. At  $\varepsilon_B \gtrsim 0.1$  the synchrotron cooling becomes dominant and the  $e^\pm$  distribution at high energies is described by the power-law  $n_e(p) \propto p^{-2}$ . A new feature appears when the magnetization is high — the bump in the electron spectrum at  $p < 10$ . This bump is a result of synchrotron self-absorption that tends to “thermalize” the high-energy pairs before they join the thermal population at low energies and thermalize via Coulomb collisions. A similar effect is seen in the spectral simulations of accreting black holes in X-ray binaries and active galaxies (Poutanen & Vurm 2009; Veledina et al. 2011).

The reduction in pair production implies a smaller Thomson optical depth ( $\tau_T \propto Y^{1/2}$ , see equation 23 in B10). As a consequence, the photospheric radius  $R_\star$  decreases with increasing  $\varepsilon_B$ . Another significant implication is the reduction in the thermal heating rate  $\dot{Q}_{\text{th}}$ , which is proportional to  $\tau_T$  (see Equation 5). Since the nonthermal injection rate  $\dot{Q}_{\text{nth}}$  remains unchanged, the ratio  $\dot{Q}_{\text{th}}/\dot{Q}_{\text{nth}}$  is reduced in magnetized jets.

The temperature of thermalized pairs remains remarkably stable as  $\varepsilon_B$  is increased (see Figure 4). This fact may be understood by noticing that even though the thermal (volume) heating rate of pairs decreases with increasing magnetization, the heating rate *per particle* does not. Note also that the thermal pairs are unable to cool via synchrotron emission because of strong self-absorption. As a result their equilibrium temperature is weakly affected by the magnetic field.

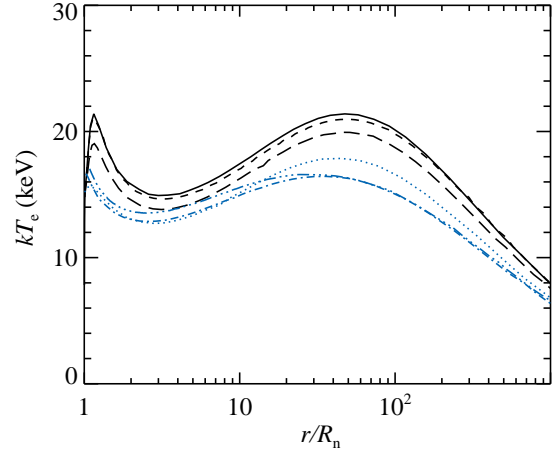


**Figure 4.** Temperature of the thermalized  $e^\pm$  population as a function of radius,  $T_e(r)$ . The jet parameters are the same as in Figure 2, except for magnetization. Different curves show models with different  $\varepsilon_B$ :  $\varepsilon_B = 0$  (solid),  $10^{-3}$  (short-dashed), 0.01 (long-dashed), 0.1 (dotted), 0.5 (dot-dashed) and 2 (triple-dot-dashed). At  $r/R_n < 10$  the temperature is set by the balance between Coulomb heating and Compton cooling; in this region  $T_e(r)$  is well described by equations (32) and (37) in B10. At larger radii, the contribution of adiabatic cooling to the thermal balance becomes non-negligible. As a result,  $T_e$  begins to slowly decrease.

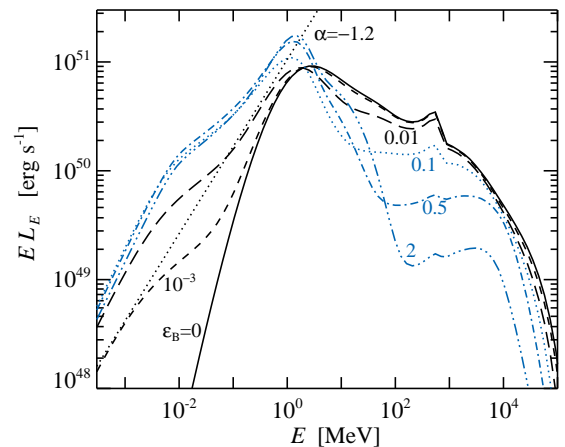


**Figure 5.** Radiation spectrum emitted by the magnetized, collisionally heated jet. The jet parameters are the same as in Figure 2, except for magnetization. The solid, short-dashed, long-dashed, dotted, dot-dashed and triple-dot-dashed curves correspond to magnetizations  $\varepsilon_B = 0, 10^{-3}, 0.01, 0.1, 0.5$  and 2, respectively. The straight dotted line shows a power-law spectrum with  $\alpha = -1.2$ . Note that the spectra shown in this figure are not corrected for the cosmological redshift  $z$ . All photons should be redshifted by the factor  $(1+z)^{-1}$ , which is  $\sim 1/3$  for a typical GRB.

## 5.2. Radiation spectrum

The spectrum that should be observed from the magnetized jet is shown in Figure 5. Magnetization significantly changes the radiative properties of the jet. It suppresses the pair cascade, reduces the photospheric radius, and changes the  $e^\pm$  distribution function. It also implies a new emission component — synchrotron emission from the nonthermal electrons and positrons.

Our detailed calculations confirm that the synchrotron radiation from strongly magnetized ( $\varepsilon_B \lesssim 1$ ), collisionally heated jets peaks at energies comparable to 1 MeV in the observer frame, as estimated in previous works (Koers & Giannios 2007; B10). The position of the synchrotron peak varies with magnetization as  $\varepsilon_B^{1/2}$ , its amplitude increases linearly with

$\varepsilon_B$  for weak magnetizations ( $\varepsilon_B \lesssim 0.01$ ) and approaches a constant value when synchrotron emission becomes the dominant energy loss mechanism for high-energy pairs. The synchrotron peak remains practically buried under the Comptonized thermal spectrum in all models shown in Figure 5. Thus, the emerging spectrum preserves the Band-type shape around the MeV peak.

The presence of synchrotron radiation significantly affects the low-energy slope of the Band peak — it makes the spectrum softer, i.e.  $\alpha$  is significantly reduced compared with the non-magnetized model. The obtained spectral shape below 1 MeV may be described as follows. The mixture of synchrotron and Comptonized thermal photons create a nearly power-law spectrum between 100 and 500 keV (with a slope  $\alpha$  that depends on  $\varepsilon_B$ ). Below this energy range, the spectrum is dominated by synchrotron radiation that has a smaller, softer slope. The resulting curvature of the spectrum may be described by observers as a soft excess above the power law. At energy  $E \sim 5$  keV the spectral slope changes again, as synchrotron self-absorption becomes important at lower energies (see Section 5.2.2).

### 5.2.1. High-energy emission

Three mechanisms contribute to emission above the MeV peak: thermal Comptonization by  $e^\pm$  pairs with temperature  $\sim 15$  keV in the jet frame, nonthermal Comptonization by the  $e^\pm$  cascade, and synchrotron emission (which extends to tens of MeV when  $\varepsilon_B$  is large).

The magnetized jets have approximately the same electron temperature  $T_e$  as non-magnetized jets, and their optical depth  $\tau_T$  is smaller. As a result, the Kompaneets' parameter  $y = 4\tau_T kT_e / m_e c^2$  is reduced with increasing  $\varepsilon_B$ . This leads to a steeper slope of the thermally Comptonized spectrum above the peak. Similar to the non-magnetized model, the thermally Comptonized power law declines at  $E \gtrsim 2\Gamma kT_e \sim 20$  MeV. In models with high  $\varepsilon_B$ , synchrotron emission makes a comparable or even dominant contribution at these energies. In the model with  $\varepsilon_B = 2$ , synchrotron emission contributes significantly to the spectrum up to 50 MeV.

The luminosity above 100 MeV is produced only by inverse Compton scattering by the nonthermal particles. This luminosity is inevitably reduced with increasing  $\varepsilon_B$ , as part of the energy of injected pairs is lost to synchrotron emission at lower energies. The nonthermal inverse Compton component becomes weaker and harder with increasing  $\varepsilon_B$ , and its slope approaches  $L_\gamma(E) \propto E^{-1/2}$ . This slope is the signature of inverse-Compton emission with suppressed pair cascade.

Overall, the suppression of the pair cascade by synchrotron cooling destroys the simple power-law shape of the high-energy spectrum. Instead, a distinct hard component (non-thermal inverse Compton) appears above 50–100 MeV.

### 5.2.2. Low-energy emission

The low-energy end of the predicted spectrum is completely dominated by synchrotron emission, even when  $\varepsilon_B$  is small (Figure 5). The spectrum at energies  $E < 5$ –10 keV is affected by self-absorption, and can be derived analytically as follows.

At any given radius  $r$ , one can define the characteristic photon energy  $E_s(r)$  below which the source is optically thick to synchrotron radiation.<sup>3</sup> As the flow expands,  $E_s$  decreases, as

does the synchrotron emissivity above  $E_s$ . The observed low-energy spectrum is in essence the superposition of emissions produced just above  $E_s$  at different radii.

In the rest frame of the plasma, the angle-averaged synchrotron emissivity and the absorption coefficient are given by (see e.g. Ghisellini & Svensson 1991)

$$j_s(\nu) = \int j_s(\nu, p) n_e(p) dp, \quad (12)$$

$$\kappa_s(\nu) = -\frac{1}{2m_e \nu^2} \int j_s(\nu, p) \gamma p \frac{d}{dp} \left[ \frac{n_e(p)}{p^2} \right] dp. \quad (13)$$

Here all quantities are measured in the plasma rest frame;  $n_e(p) = n_+(p) + n_-(p)$  is the distribution function of  $e^\pm$  pairs, and  $j_s(\nu, p)$  is the angle-averaged synchrotron emissivity per electron. For analytical estimates we will use the delta-function approximation for the emissivity

$$j_s(\nu, p) = \frac{1}{4\pi} \frac{4}{3} c \sigma_T U_B p^2 \delta(\nu - \gamma^2 \nu_B), \quad (14)$$

where  $\nu_B = eB/2\pi m_e c$  is the Larmor frequency.

The particles responsible for the partially self-absorbed emission are in the nonthermal tail of the  $e^\pm$  distribution, which we approximate as a power-law  $n_e(p) = Ap^{-\delta}$ . Then Equations (12)–(14) give (Rybicki & Lightman 1979)

$$j_s(\nu) = \frac{A}{6\pi \nu_B} c \sigma_T U_B \left( \frac{\nu}{\nu_B} \right)^{-(\delta-1)/2}, \quad (15)$$

$$\kappa_s(\nu) = \frac{2\pi^2}{9} (\delta + 2) A \frac{e}{B} \left( \frac{\nu}{\nu_B} \right)^{-(\delta+4)/2}. \quad (16)$$

The  $e^\pm$  density in the collisionally heated jet scales with radius as  $r^{-2}$  (B10). The proton density  $n$  also scales as  $r^{-2}$ . This implies

$$A \propto r^{-2}, \quad B = \sqrt{8\pi \varepsilon_B n m_p c^2} \propto r^{-1}, \quad \nu_B \propto r^{-1}. \quad (17)$$

The characteristic optical depth to self-absorption at a given photon energy  $\nu$  is given by

$$\tau_s(\nu, r) \propto \int_r^\infty \kappa_s(\nu) dr \propto r \kappa_s(\nu) \propto (\nu r)^{-(\delta+4)/2}. \quad (18)$$

Setting  $\tau_s(\nu) = 1$  we find that the self-absorption energy  $\nu_s$  scales as

$$\nu_s \propto r^{-1}. \quad (19)$$

From Equations (16), (17), and (18) we also find

$$\frac{\nu_s}{\nu_B} = \gamma_s^2 = \text{constant}, \quad (20)$$

where  $\gamma_s$  is the Lorentz factor of the pairs emitting near the self-absorption frequency; it remains constant along the jet. The value of  $\gamma_s$  is a weak function of the magnetization  $\varepsilon_B$  and varies between 10 and 15 for the cases considered here.

The emissivity near the self-absorption frequency can be read from Equation (15), setting  $\nu = \nu_s$ . Using (17) and (20) we find

$$j_s(\nu_s) \propto r^{-3}. \quad (21)$$

<sup>3</sup> The *intrinsic* spectrum at  $E < E_s$  has the photon index  $\alpha = 3/2$ , characteristic of a power-law electron distribution producing the self-absorbed emission, see Equations (15) and (16) and Rybicki & Lightman (1979).

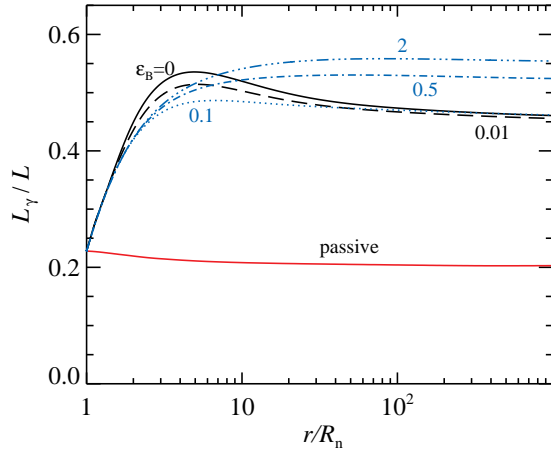


**Figure 6.** Fraction of the flow energy carried by radiation as a function of distance from the central source, for different magnetizations:  $\varepsilon_B = 0$  (solid line), 0.01 (long-dashed), 0.1 (dotted), 0.5 (dot-dashed) and 2 (triple-dot-dashed). For comparison, the radiative efficiency for a passively cooling flow is also plotted (lower solid line).

For the optically thin synchrotron emissivity at  $\nu > \nu_s$  we may write

$$j_s(\nu) = j_s(\nu_s) \left( \frac{\nu}{\nu_s} \right)^{-(\delta-1)/2}. \quad (22)$$

Now let us define the synchrotron absorption radius  $R_s(E)$  for photons of a given energy  $E$  in the static (observer) frame, which corresponds to  $h\nu = E/D$ . Neglecting the self-absorbed radiation from  $r < R_s$ , we estimate the observed synchrotron luminosity  $L_s(E)$  by integrating the synchrotron emissivity over the optically thin region  $r > R_s(E)$ ,

$$L_s(E) \approx \int_{R_s(E)}^{\infty} C \frac{4\pi}{h} j_s(\nu) 4\pi r^2 dr, \quad (23)$$

where we approximate  $h\nu \approx E/\Gamma$  and use the fact that the angle-integrated emissivity  $j_s$  is the same in the static and co-moving frames within a factor  $C \sim 1$ .<sup>4</sup> It is straightforward to evaluate the integral in Equation (23) using Equation (22). This gives

$$L_s(E) \propto E^0. \quad (24)$$

The integral (23) peaks near  $R_s$  and Equation (24) in essence states that emissivity  $j_s(\nu)$  at radius  $R_s$  satisfies  $R_s^3(\nu)j_s(\nu) = \text{const}$ . This condition can also be inferred from Equation (21) without calculating the integral.

We conclude that the low-energy ( $E \ll 5$  keV) emission from collisionally heated jets has the energy spectrum  $EL_\gamma(E) \propto E$  which corresponds to photon index  $\alpha = -1$ . This analytical result is consistent with the numerically calculated spectra in Figure 5. The predicted low-energy spectrum extends to the optical band with a constant slope. Thus, significant prompt optical emission is expected from collisionally heated jets.

<sup>4</sup> For the radiation spectrum given by Equation (22), this factor is

$$C = \frac{1}{2} \int_{-1}^1 \left( \frac{D}{\Gamma} \right)^{\frac{\delta-1}{2}} d\mu \approx \frac{1}{2} \int_{-1}^1 (1+\mu)^{\frac{\delta-1}{2}} d\mu = \frac{2^{\frac{\delta+1}{2}}}{\delta+1}.$$

### 5.3. Radiative efficiency

The radiative efficiency of the jet  $\varepsilon_{\text{rad}}$  is defined as the ratio of the photon luminosity  $L_\gamma$  to the kinetic luminosity of the plasma outflow  $L$ . Note that  $L(r) \approx \text{const}$  for the matter-dominated jet and  $L_\gamma$  evolves with radius. This evolution is shown in Figure 6. The final efficiency is given by the asymptotic value of  $\varepsilon_{\text{rad}} = L_\gamma/L$  at large radii.

The photon luminosity prior to the onset of dissipation ( $r = R_n$ ) is found from the passively cooling jet model. One can see from Figure 6 that  $L_\gamma$  is greatly increased by the intense collisional heating at  $r \gtrsim R_n$ . The net energy given to radiation by collisional heating outside a given radius is obtained by integrating Equations (3) and (5) over volume; the result is proportional to  $r^{-1}$ . Thus, heating peaks near  $R_n$  and continues with a smaller rate at larger radii. On the other hand,  $L_\gamma$  is reduced by adiabatic cooling, in particular in the opaque zone  $r < R_*$ . The competition between collisional heating and adiabatic cooling shapes  $L_\gamma(r)$ . In weakly magnetized jets, the photospheric radius is large,  $R_* \sim 20R_n$ , and adiabatic cooling is more efficient. It begins to win over collisional heating at  $r \sim 5R_n$  and somewhat reduces  $L_\gamma$ . In strongly magnetized jets, the photospheric radius  $R_*$  is smaller because the magnetic field suppresses the production of  $e^\pm$  pairs (Section 5.1). In this case, adiabatic cooling is less efficient.

In all cases shown in Figure 6 the final  $\varepsilon_{\text{rad}}$  is close to 50%. We conclude that the radiative efficiency of collisionally heated jets remains high for the entire range of  $\varepsilon_B$  considered in this paper.

## 6. DISCUSSION

Only two radiative processes are in principle capable of producing the GRB spectrum with an extended high-energy tail: synchrotron emission and Comptonization. These are two basic modes of energy transfer from a heated plasma to radiation, and their theory was developed long ago. In particular, the formation of photospheric spectra through Comptonization in X-ray sources was investigated in the 1970s, with various applications from accretion disks to the expanding Universe (see e.g. Pozdnyakov et al. 1983). Comptonization in GRBs has been discussed for about two decades (see Section 6.2 below). Besides the fact that subphotospheric heating creates a nonthermal-looking radiation spectrum, one would like to know what the heating process is. Answering this question can help disentangle the GRB physics — the nature and composition of the jet and the central engine.<sup>5</sup> Progress in this direction was hampered for many years by the complexity of collisionless processes that were usually invoked in GRB production.

GRB spectra can be shaped by three possible heating mechanisms: (1) collisionless shocks, (2) magnetic dissipation, and (3) collisional dissipation. Least understood is magnetic dissipation, and it is usually modeled by introducing phenomenological parameters. A similar phenomenological approach was used for internal shocks in the jet until recent numerical simulations began to provide insights into shock physics. Collisional dissipation is the most straightforward mechanism of these three. It can be calculated exactly, from first principles. B10 recently showed that collisional heating possesses the key features of a successful GRB mechanism: efficient

<sup>5</sup> The situation may be compared with X-ray binaries, where Comptonization is thought to occur in a corona of the accretion disk or the inner hot flow, and the main puzzle is how the plasma is heated.

electron heating, high radiative efficiency and, most importantly, it generates the observed Band-type spectrum.

In this paper, we calculated the emission from collisionally heated jets by solving the time-dependent, coupled kinetic equations for the particle and photon distributions inside the jet. The advantage of our numerical code is the accurate modeling of all relevant kinetic and radiative processes including Coulomb collisions and synchrotron self-absorption. It allowed us to systematically explore the effects of jet magnetization on the emerging spectrum. We calculated the emerging radiation using the equation of radiative transfer (B11) instead of the Monte-Carlo method used by B10. The only disadvantage of our code is that it uses angle-averaged coefficients of emission and absorption in the transfer equation. Comparison with exact transfer models of B10 and B11 shows that this approximation is reasonable, in particular at photon energies below GeV. Note also that this is the first implementation of radiative transfer calculations in a kinetic GRB code. The previously developed kinetic codes assumed isotropy of radiation in the rest-frame of the plasma (Pe’er & Waxman 2005; VP09), which is invalid in the main region of interest  $\tau_T < 10$ .

### 6.1. Spectra from non-magnetized and magnetized jets

First, we calculated the emission from the fiducial baryonic jet model of B10 with zero magnetic field ( $\varepsilon_B = 0$ ). Our results agree with B10: the spectrum peaks at 1 MeV, has the low-energy photon index  $\alpha \approx 0.4$  and the high-energy photon index  $\beta \approx -2.5$ . We conclude that the Band-type spectrum is a robust prediction of the collisional-heating model. Similar to B10, we stress the *ab initio* character of our calculations: the dissipation process and generated radiation are derived from first principles, without introducing any phenomenological parameters for the heating mechanism.

The collisional heating peaks below the photosphere, where the  $\gamma$ - $\gamma$  opacity is large for multi-GeV photons emitted in the  $e^\pm$  cascade. The nuclear collisions also occur at much larger radii (although with a smaller rate) where the  $\gamma$ - $\gamma$  optical depth is reduced and the high-energy photons can escape. As a result, instead of a cutoff at a few GeV, the predicted spectrum exhibits a moderate steepening at  $\sim 5$  GeV and extends up to  $\sim 100$  GeV (Figure 2). A similar behavior is seen in the Monte-Carlo results of B10, with somewhat smaller normalization of the multi-GeV emission. This difference must be caused by the angle-averaged approximation for  $j_\nu$  and  $\kappa_\nu$  that was adopted in our calculations of radiative transfer. As discussed above, the accuracy of this approximation is reduced at photon energies  $E > 1$  GeV.

Secondly, we calculated the emission from magnetized jets with collisional heating. We considered the range of magnetization parameters  $0 < \varepsilon_B < 2$ , so the magnetic energy was at most comparable to the energy of the baryonic component. We did not consider magnetically dominated jets with  $\varepsilon_B \gg 1$  for two reasons. First, the strong magnetic field can change the jet dynamics. Then the coasting approximation (which is reasonable for a matter-dominated jet) would be invalid. Second, the strongly magnetized case is computationally more difficult. The generated spectra in this regime are left for a future study.

Our calculations show that magnetization has a small effect on the position of the spectral peak  $E_{\text{peak}}$  — it is only slightly shifted to lower energies. The spectrum still has the Band-type shape around the peak, with  $\alpha$  and  $\beta$  depending on  $\varepsilon_B$  (Figure 5 and Table 1). Magnetization significantly affects the

shape of the spectrum at high ( $E \gg E_{\text{peak}}$ ) and low ( $E \ll E_{\text{peak}}$ ) energies.

The high-energy emission is reduced with increasing  $\varepsilon_B$  (Figure 5), because the nonthermal  $e^\pm$  generated by nuclear collisions emit less via inverse Compton scattering and more at low energies via the synchrotron mechanism. This change is significant if  $\varepsilon_B \gg 10^{-2}$ . Synchrotron cooling of the injected high-energy  $e^\pm$  has a throttling effect on the pair cascades. As a result, magnetized jets have smaller densities of  $e^\pm$  pairs and a smaller photospheric radii  $R_*$ .

The low-energy emission is increased with increasing  $\varepsilon_B$ . An important effect of magnetization is the softening of the spectral slope below  $E_{\text{peak}}$ . This is the result of synchrotron emission from nonthermal pairs. At energies below  $\sim 30$  keV a clear soft excess is predicted, even for small  $\varepsilon_B \sim 10^{-3}$ . Our model also predicts that the spectrum below a few keV should have the photon index  $-1$ . This spectrum extends down to the optical band.

Note that photon spectra in this paper are not corrected for the cosmological redshift  $z$ . The actually observed energy of all photons is smaller by the factor of  $(1+z)^{-1}$ . In particular, the soft excess is redshifted to  $\sim 10$  keV for a typical  $z$  of GRBs.

### 6.2. Comparison with other models of subphotospheric Comptonization

Thompson (1994) proposed that GRB photons are Comptonized in the subphotospheric region by turbulent bulk motions of the plasma in the jet. His model assumed that the jet is dominated by magnetic field and pictured Alfvénic turbulence generated by some instabilities (e.g. by reconnection). Building a detailed theory of turbulence from first principles would be a formidable task, and Thompson (1994) made estimates assuming that the plasma motions are limited by radiation drag. Then the bulk Comptonization occurs in the unsaturated regime and controlled by the efficiency of turbulence generation against the drag. The predicted GRB spectrum is sensitive to this unknown efficiency, which may vary with radius. The mechanism is very different from collisional heating. Direct comparison of the model predictions is difficult, because Thompson (1994) used the theory of Comptonization in static sources, which is not valid for GRBs (see discussion in Section 3). Like in the expanding Universe, the number of scatterings in a GRB jet scales as  $\sim \tau_T$  (not as  $\tau_T^2$ ) and is controlled by the decrease in density, not the escape of photons from the plasma.<sup>6</sup> The expected spectrum can only be found by solving radiative transfer in the expanding jet, and we emphasize the importance of accurate transfer calculations for GRB models.

Mészáros & Rees (2000b) and Rees & Meszaros (2005) discussed subphotospheric Comptonization in general terms and highlighted its importance for GRBs. They argued that Comptonization helps explain observations, although they did not consider any concrete model. More detailed calculations were performed by Pe’er et al. (2006). They still did not focus on any concrete physical scenario and experimented with various phenomenological models, using free parameters to describe the heating process: the amount of dissipated energy and its fraction that is given to electrons, the shape of the electron distribution, and the optical depth at which the

<sup>6</sup> If collisional heating occurred in a static source, the emerging spectrum would have two peaks, resembling the Comptonized spectra of accretion-disk corona. In contrast, the spectrum emitted by the GRB jet has only one peak.

dissipation occurs. Various combinations of these parameters led to various spectra. In contrast, we investigated the concrete physical model of collisional dissipation, which predicts the thermal and nonthermal heating rates, both scaling as  $r^{-1}$ . It is therefore hard to compare their results with ours. We can only compare the technical tools. Pe’er et al. (2006) used the kinetic code developed by Pe’er & Waxman (2005). In many respects, their code is similar to ours, except one difference: their code assumes that radiation is isotropic in the comoving frame of the jet. We gave up this approximation because of its inadequacy at the relevant modest optical depths (see Section 3) and instead solved the radiative transfer equation. Note also that Pe’er et al. (2006) argued that GRB jets never become dominated by  $e^\pm$  pairs. In contrast, we find that jets with magnetization  $\varepsilon_B \ll 1$  have a large pair loading factor  $n_e/n \sim 20 - 40$ , which changes the position of the photosphere by the factor of 20–40.

Giannios (2006) investigated Comptonization in jets that carry alternating magnetic fields and are heated by magnetic reconnection (Drenkhahn & Spruit 2002). This model has two phenomenological parameters — the reconnection rate and the fraction of dissipated energy that is deposited into electrons. The effect of magnetic dissipation on the electron distribution is unknown. Giannios (2006) assumed a thermal electron distribution and studied the radiation produced by this model. He used a Monte-Carlo code and an iterative technique to simulate the radiative transfer in the jet.<sup>7</sup> We note that the jet model in Giannios (2006) is significantly different from B10 and our work. In particular, the jet continues to accelerate as  $\Gamma \propto r^{1/3}$  in the heated subphotospheric region while we focus on matter-dominated jets with  $\Gamma \approx const.$  The electron temperature scales with radius approximately as  $T_e \propto r^{5/3}$  while in our model we find that  $T_e$  varies only by a factor of  $\sim 2$  for three decades in radius (Figure 4). Note also that Giannios (2006) assumed pure thermal heating, leading to negligible pair creation. In contrast, our work and B10 predict a nonthermal  $e^\pm$  cascade, which has important effects on the observed spectrum at high energies (above 10 MeV) and at low energies where synchrotron emission from the cascade becomes dominant.

Lazzati & Begelman (2010) considered a simplified model for Comptonization following an impulsive heating event below the photosphere. In their model, all electrons in a slab of optical depth  $\tau_T \sim 2$  are suddenly given a Lorentz factor  $\gamma$  and then cooled by blackbody radiation. This setup can produce a variety of photon spectra depending on photon-to-electron ratio  $n_\gamma/n_e$ ,  $\tau_T$ , and  $\gamma$ . It has, however, a problem. The sudden heating of the slab (faster than Compton cooling) can hardly describe any physical dissipation mechanism, as different parts of the slab are causally disconnected. The causal contact (light-crossing) time for a region with  $\tau_T \sim 2$  is orders of magnitude longer than Compton cooling time.

### 6.3. Comparison with observed GRB spectra

The main part of observed GRB radiation is emitted with a Band-type spectrum — a smoothly broken power law that peaks near 0.3 MeV. The spectral slopes below and above the peak ( $\alpha$  and  $\beta$ ) vary (Preece et al. 2000). The most frequently measured low-energy slope  $\alpha$  is close to  $-1$ , but in some cases

it reaches 1 (Rayleigh-Jeans slope of the Planck spectrum). The most frequently measured high-energy slope  $\beta$  is near  $-2.5$ ; it also significantly varies from burst to burst, roughly between  $-2$  and  $-3$ .

The spectra predicted by our model appear to agree with observations. The predicted spectral peak is close to  $\text{MeV}/(1+z)$ . The average observed values of  $\alpha \sim -1$  and  $\beta \sim -2.5$  are consistent with the collisionally heated jet with magnetization  $\varepsilon_B \sim 10^{-3} - 10^{-2}$ . A lower magnetization  $\varepsilon_B < 10^{-3}$  leads to harder  $\alpha$  up to 0.4. Larger slopes are not expected from the matter-dominated jets. The slope  $\alpha = 1$  is predicted only in the radiation-dominated regime — in this case the jet emits a Planckian spectrum (B11).

It should be noted that our calculations give practically *instantaneous* observed spectra. The main part of the prompt emission (photon energies from soft X-rays to a few GeV) is dominated by the photosphere in our model. The emission is produced by a sequence of short-lived (in observer time) independent emitters passing through  $R_*$  — the sequence of shells of thickness  $\delta r \lesssim R_*/\Gamma^2$ , which corresponds to duration  $\delta t_{\text{obs}} \sim 10^{-4}$  s for typical parameters of GRB jets. The spectra obtained by modern detectors do not provide this high temporal resolution, because of insufficient photon statistics. The observed spectra must be a mixture of emissions from different shells, possibly with significant variations in  $L$  and  $E_{\text{peak}}$ . The superposition of different instantaneous spectra generally tends to reduce the observed slope  $\alpha$  and can give  $\alpha \sim -1$  even for non-magnetized jets (R. Mochkovitch, in preparation).

An interesting feature of the magnetized model of collisionally heated jet is the soft excess that appears at energies  $\sim 30(1+z)^{-1}$  keV. It may provide an explanation for the X-ray excesses that have been observed in several bursts (Preece et al. 1996), including the recent example of GRB 090902B (Abdo et al. 2009a).

Prompt optical emission is expected from collisionally heated jets, with a slope  $L_\gamma(E) = const$  (photon index  $-1$ ). This emission peaks at the self-absorption radius  $R_s(E) \gg R_*$  and should be observed with a time lag  $\sim R_s/c\Gamma^2 \sim 1$  s with respect to the MeV radiation that is released at  $r \sim R_*$ . The prompt optical emission has been detected in some GRBs, but the data are sparse, as prompt optical observations are difficult. In some cases (e.g. GRB 080319B) the optical luminosity appears to exceed the predictions of our model, suggesting an additional source of emission (e.g. shocks or neutron decay, see B10).

The high-energy index  $\beta$  predicted by the collisional model can easily be steeper than  $-2.5$ , because of a large  $\varepsilon_B$  (Figure 5) or less efficient heating (B10). The model can also accommodate very hard slopes  $\beta > -2$  that are observed in some GRBs (see e.g. Figure 7 in B10).

Our model predicts significant multi-GeV emission, especially when  $\varepsilon_B$  is small. It implies that the prompt GRB emission can contribute to the radiation observed by LAT instrument of the *Fermi* telescope. The prompt high-energy photons should mix together with radiation from the other, long-lived, high-energy source that was identified by LAT in a fraction of GRBs and whose origin is debated.

Overall, our results support the view that the main peak of GRB spectra is dominated by photospheric radiation of the ultra-relativistic jet from the central engine. Note that photospheric emission is often erroneously pictured as a Planckian component in GRB spectra. As shown in B11, the pho-

<sup>7</sup> The basic numerical methods used by Giannios (2006) and B10 are similar, except that the iterations of the electron temperature in Giannios (2006) are simplified: the profile  $T_e(r)$  is searched in the power-law form, with two parameters to iterate — the normalization and the slope of the power law.

photospheric spectrum has a Planckian shape only if the jet energy is strongly dominated by radiation at  $R_*$ . This radiation-dominated regime requires an extremely high Lorentz factor, which corresponds to a very baryon-poor jet. Baryon-dominated jets cannot produce Planckian spectra, even if the jet experiences no dissipation and only emits adiabatically cooled thermal photons from the photosphere (Figure 1 in B10). In reality, the jet should experience strong collisional dissipation, which has a huge impact on its photospheric ra-

diation and makes it even more different from Planckian. The only feature shared with Planckian radiation is the single spectral peak at  $E_{\text{peak}} \sim 1$  MeV. The photospheric spectrum of the collisionally heated jet is much broader than Planckian and fits the observed GRBs.

This work was supported by the Wihuri foundation and ERC Advanced Research Grant 227634 (IV), NSF grant AST-1008334 and NASA grant NNX10AO58G (AMB), and the Academy of Finland grant 127512 (JP).

#### APPENDIX

##### RADIATIVE TRANSFER

Equation (7) is valid for relativistic outflows in the limit  $\Gamma \rightarrow \infty$ . For finite  $\Gamma \gg 1$ , the equation accurately describes the transfer in a steady jet. Its accuracy is reduced if the jet is variable on scales  $\delta r \lesssim r/\Gamma^2$ , as discussed in B11. Here we give a more formal discussion of transfer in variable jets and the applicability of the steady equation (7). The general equation of radiative transfer in a spherically symmetric outflow with any Lorentz factor  $\Gamma(t, r)$  can be written as (Mihalas 1980)

$$\widehat{\mathcal{L}}I_\nu = \left[ \frac{\Gamma\beta}{r}(1-\mu^2) + \frac{\mu}{\beta\Gamma} \widehat{\mathcal{L}}\Gamma \right] \nu^3 \frac{\partial}{\partial \ln \nu} \left( \frac{I_\nu}{\nu^3} \right) - (1-\mu^2) \left[ \frac{\Gamma}{r}(1+\beta\mu) - \frac{1}{\beta\Gamma} \widehat{\mathcal{L}}\Gamma \right] \frac{\partial I_\nu}{\partial \mu} + j_\nu - \kappa_\nu I_\nu, \quad (\text{A1})$$

where  $\widehat{\mathcal{L}}$  is the differential operator

$$\widehat{\mathcal{L}} = \Gamma(1+\beta\mu) \frac{\partial}{c\partial t} + \Gamma(\mu+\beta) \frac{\partial}{\partial r}. \quad (\text{A2})$$

Here  $\beta = (1 - \Gamma^{-2})^{1/2}$  is the flow velocity in units of  $c$ ,  $t$  and  $r$  are time and radial coordinate measured in the static frame, whereas the cosine  $\mu$  of the photon angle relative to the radial direction, the specific intensity  $I_\nu$ , the emission and absorption coefficients  $j_\nu$  and  $\kappa_\nu$  are all measured in the local comoving frame.

Let us define a coordinate  $s$  by the following implicit relation

$$s = ct - \frac{r}{\beta(s)}. \quad (\text{A3})$$

For a matter-dominated (coasting) flow,  $\Gamma(s) \approx \text{const}$  and  $s$  can serve as a Lagrangian coordinate that labels different shells of the flow, as  $s = \text{const}$  along the worldlines of the shells. Changing variables  $r, t \rightarrow r, s$ , we rewrite the operator (A2) as

$$\widehat{\mathcal{L}} = \Gamma(\mu+\beta) \frac{\partial}{\partial r} - \frac{\mu}{\beta\Gamma} \left[ 1 - \frac{r}{\beta^3\Gamma^2} \frac{d \ln \Gamma}{ds} \right]^{-1} \frac{\partial}{\partial s}. \quad (\text{A4})$$

Here the spatial derivative  $\partial/\partial r$  is taken along the worldline (i.e. at  $s = \text{const}$ ). Note that the flow worldlines do not cross (i.e. there are no caustics) as long as the bracket in Equation (A4) is non-zero.

If the flow varies on scales  $\delta r \sim r/\Gamma^2$ , the two parts of the operator (A4) are comparable. The problem simplifies (becomes formally equivalent to the steady problem) if the flow varies on scales much larger than  $r/\Gamma^2$ . Then the operator  $\widehat{\mathcal{L}}$  is dominated by the first term that is proportional to  $\partial/\partial r$ . The left-hand side of Equation (A1) simplifies to  $\widehat{\mathcal{L}}I_\nu = \Gamma(\mu+\beta) \partial I_\nu/\partial r$ . Similarly, the right-hand side of Equation (A1) simplifies and the transfer equation becomes,

$$\frac{1}{r^2} \frac{\partial}{\partial \ln r} [(\mu+\beta) r^2 I_\nu] = \frac{r}{\Gamma} (j_\nu - \kappa_\nu I_\nu) + \beta(1-\mu^2) \frac{\partial I_\nu}{\partial \ln \nu} - \frac{\partial}{\partial \mu} [(1-\mu^2)(1+\beta\mu) I_\nu], \quad (\text{A5})$$

which becomes Equation (7) for outflows with  $\beta \approx 1$ . Formally, this is achieved simply by replacing  $\partial/\partial r|_t$  by the derivative along the flow worldline  $\partial/\partial r|_s$ . Equation (A5) can also be written using the flow proper time as the independent variable,  $t = r/c\beta\Gamma$ .

#### REFERENCES

- Abdo A. A. et al. 2009a, *ApJ*, 706, L138  
—, 2009b, *Science*, 323, 1688  
Bahcall, J. N., & Mészáros, P. 2000, *Phys. Rev. Lett.*, 85, 1362  
Beloborodov, A. M. 2003, *ApJ*, 588, 931  
—, 2008, in *AIP Conf. Ser.* 1054, *Cool Discs, Hot Flows: The Varying Faces of Accreting Compact Objects*, ed. M. Axelsson (Melville, NY: AIP), p. 51  
—, 2010, *MNRAS*, 407, 1033 (B10)  
—, 2011, *ApJ*, submitted (arXiv:1011.6005) (B11)  
Chandrasekhar, S. 1960, *Radiative Transfer* (New York: Dover)  
Daigne, F., Bosnjak, Z., & Dubus, G. 2011, *A&A*, 526, A110  
Derishev, E. V., Kocharovskiy, V. V., & Kocharovskiy, V. V. 1999, *ApJ*, 521, 640  
Drenkhahn, G., & Spruit, H. C. 2002, *A&A*, 391, 1141  
Fuller, G. M., Pruet, J., & Abazajian, K. 2000, *Phys. Rev. Lett.*, 85, 2673  
Ghisellini, G., & Svensson, R. 1991, *MNRAS*, 252, 313  
Giannios, D. 2006, *A&A*, 457, 763  
Ginzburg, V. L., & Syrovatskii, S. I. 1964, *The Origin of Cosmic Rays* (New York: Macmillan)  
Goodman, J. 1986, *ApJ*, 308, L47

- Imshennik, V. S., Nadezhin, D. K., & Pinaev, V. S. 1967, *Soviet Ast.*, 10, 970
- Koers, H. B. J., & Giannios, D. 2007, *A&A*, 471, 395
- Lazzati, D. & Begelman, M. C. 2010, *ApJ*, 725, 1137
- Mészáros, P., & Rees, M. J. 2000a, *ApJ*, 541, L5
- . 2000b, *ApJ*, 530, 292
- Mihalas, D. 1980, *ApJ*, 237, 574
- Paczynski, B. 1986, *ApJ*, 308, L43
- . 1990, *ApJ*, 363, 218
- Paczynski, B., & Xu, G. 1994, *ApJ*, 427, 708
- Pe'er, A., Mészáros, P., & Rees, M. J. 2006, *ApJ*, 642, 995
- Pe'er, A., & Waxman, E. 2005, *ApJ*, 628, 857
- Piran, T., Shemi, A., & Narayan, R. 1993, *MNRAS*, 263, 861
- Poutanen, J., & Vurm, I. 2009, *ApJ*, 690, L97
- Pozdnyakov, L. A., Sobol, I. M., & Sunyaev, R. A. 1983, *Sov. Sci. Rev. E, Astrophys. Space Phys.* (ed. R.A. Sunyaev), 2, 189 (New York: Harwood Academic Publishers)
- Preece, R. D., Briggs, M. S., Pendleton, G. N., Paciesas, W. S., Matteson, J. L., Band, D. L., Skelton, R. T., & Meegan, C. A. 1996, *ApJ*, 473, 310
- Preece, R. D., Briggs, M. S., Mallozzi, R. S., Pendleton, G. N., Paciesas, W. S., & Band, D. L. 2000, *ApJS*, 126, 19
- Rees, M. J., & Meszaros, P. 1994, *ApJ*, 430, L93
- . 2005, *ApJ*, 628, 847
- Rossi, E. M., Beloborodov, A. M., & Rees, M. J. 2006, *MNRAS*, 369, 1797
- Rybicki, G. B., & Lightman, A. P. 1979, *Radiative Processes in Astrophysics* (New York: Wiley-Interscience)
- Sironi, L., & Spitkovsky, A. 2009, *ApJ*, 698, 1523
- . 2011, *ApJ*, 726, 75
- Stern, B. E., & Poutanen, J. 2004, *MNRAS*, 352, L35
- Svensson, R. 1987, *MNRAS*, 227, 403
- Thompson, C. 1994, *MNRAS*, 270, 480
- Veledina, A., Vurm, I., & Poutanen, J. 2011, *MNRAS*, in press [arxiv: 1012.0439]
- Vurm, I., & Poutanen, J. 2009, *ApJ*, 698, 293 (VP09)
- Zhang, B. B., Zhang, B., Liang, E. W., Fan, Y. Z., Wu, X. F., Pe'er, A., Maxham, A., Gao, H., & Dong, Y. M. 2011, *ApJ*, 730, 141